

A floating connector element formulation for multi-level modelling of composite structures

E.S. Kocaman^{a,1,*}, B.Y. Chen^b, S.T. Pinho^a

^a*Department of Aeronautics, South Kensington Campus, Imperial College London. London SW7 2AZ, United Kingdom*

^b*Faculty of Aerospace Engineering, Delft University of Technology. Kluyverweg 1, 2629 HS Delft, Netherlands*

Abstract

Design and optimisation of large structures, including the positioning of lower-level components, typically require extensive user involvement and sequential mechanical analysis/optimisation iterations. This paper presents an original method that enables adaptive positioning of lower-level models (such as components) within higher level-models (such as large structures), and that achieves a combined mechanical/optimisation problem for the design of structures with various hierarchical levels (such as the positioning of stiffeners within a wingbox). As the position of the lower-level model evolves, our proposed method does not require re-generating of the geometry, remeshing or modifying the stiffness matrix of the elements corresponding to the various hierarchical levels. Instead, we achieve the adaptive positioning via an original concept that we propose here: Floating Connector (FC) elements. In this paper, we validate the FC elements against reference purely-mechanical solutions, show that they can be combined with gradient-descent method and genetic algorithms, and that they can be applied to optimise the positioning of a stiffener runnout taking into account a debonding manufacturing defect.

Keywords:

Multi-level modelling, Structural design, Optimization, Composites

*Corresponding author

Email address: e.kocaman15@imperial.ac.uk (E.S. Kocaman)

¹Tel: +44 7887816544. Address: Department of Aeronautics, South Kensington Campus, Imperial College London, London SW7 2AZ, UK.

1. Introduction

1.1. Background

In the design of large engineering structures, such as wing-boxes in aircraft, it is often the case that structural details, such as stiffeners, need to be designed and positioned during the design of the overall structure.

The current practice for the numerical design of these large structures with structural details involves creating large (yet typically coarse) finite element (FE) models of the large structure, as well as detailed models of the structural details, assuming a certain configuration. Eventually, these two models may be used in a multi-level framework.

Within the multi-level framework, there are various iterative [1–7] and concurrent [8–16] methods in the literature to include a structural detail into a larger model. In iterative (sub-modelling) approaches, a global and a local model are simulated separately within an iterative procedure. The results from one model are used to calculate the appropriate boundary conditions for the other model, until convergence is achieved. In concurrent approaches, structural details are directly integrated to the large model and the overall system is simulated simultaneously.

For optimising the positioning (or other characteristics) of the components, various approaches can be followed [15–22]. For instance, the software used for the mechanical analysis can then be used iteratively with an optimisation software. Alternatively, various mechanical FE models corresponding to various configurations that span the entire design space can be created and ran, and the optimisation can then be done using surrogate models [17–20] that use the sampled simulation data.

When proceeding as described above for the design of large engineering structures, there is typically a substantial investment required for creating each FE model for each new configuration of the large structure: in terms of the effort required of the modeller, the time it takes to create each new new (CAD and) FE model, and the associated financial cost. Alternatively, a significant investment can instead go towards creating a parametric mesh that can generate various configurations automatically. In either case, defining an optimal configuration then requires iterating between independent FE and optimisation software codes (some of this iteration can be automated via dedicated via dedicated software packages such as Isight [23]).

As a consequence of the above, detailed FE models of large structures are typically built only very late in the design stage, once many design decisions have already been frozen. Therefore, effective simulation methodologies that enable combined mechanical FE and optimisation analyses of large structures, allowing for the positioning (or other characteristics) of structural details to be defined during the analysis, would be key to enable an early use of numerical simulation during the design process.

Ideally, from the designer’s point of view, a full numerical model of a large structure would not rigidly represent just one single configuration, but would instead be equally compatible with any number of con-

35 configurations (Figure 1), with the parameters defining each configuration being themselves variables to be
36 determined in a single combined mechanical / optimisation analysis.

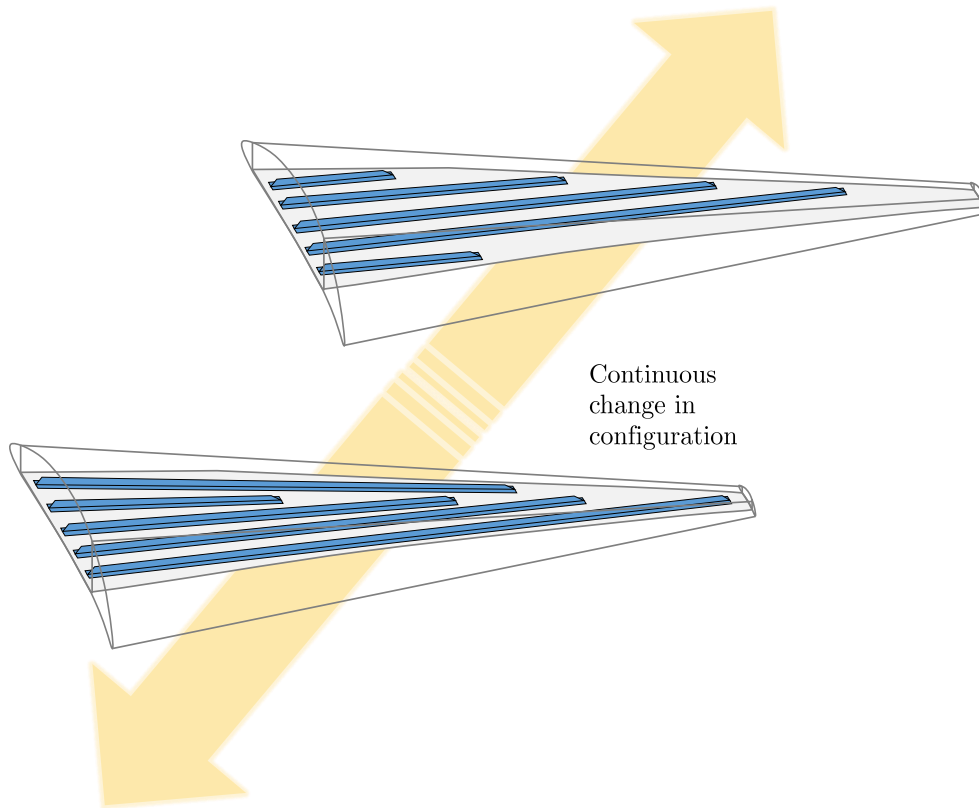


Figure 1: The full FE model of a large structure allows for the precise configuration to be defined during (and by) the solution process

37 1.2. Objective, novelty and outline

38 In this paper, we derive a new numerical framework for multi-level design of large structures, where
39 design variables associated with sub-structures (e.g. the positioning of a component) are solved for in a
40 numerical optimisation problem concurrently with the variables associated with the mechanical problem
41 (displacements).

42 This numerical framework is underpinned by an original element type, which we present in this paper and
43 call 'Floating Connector (FC) element', that can be used to connect sub-structures (i.e. components such
44 as stiffeners) to an underlying large structure (e.g. a wing) without locking their relative position. Instead,
45 this relative position is defined during the analysis itself via an optimisation code 'inside' the element.

46 This new element type constitutes a step change in the literature, in that it allows us to integrate
47 different hierarchical levels of a structural model adaptively, without going through costly geometry and
48 mesh generation as the configuration evolves, and in that it allows us to solve the optimisation problem

49 concurrently with the mechanical problem. Additionally, we will show that FC elements also provide an
 50 improved platform for investigating the effect of various manufacturing defects (such as debonding between
 51 a stiffener and a skin).

52 The element description and formulation is presented in Section 2. Section 3 contains verification of the
 53 floating connection, while Section 4 contains verification of the concurrent optimisation capabilities. The
 54 application of the element for skin-stiffener debonding investigation is demonstrated in Section 5 followed
 55 by Section 6 where the implications of the results are discussed and the overall conclusions are summarized
 56 in Section 7.

57 **2. Development of a *floating connector* methodology**

58 *2.1. Element description*

59 The proposed element topology incorporates all the nodes along the interacting surfaces of the two bodies
 60 (that need to be connected) into one floating connector element (see Figure 2). This element contains floating
 61 connectors which introduce multi-point constraints (MPCs) between suitable Degrees of Freedoms (DoFs)
 62 that can be selected adaptively using a suitable optimization algorithm. The implementation of the element
 63 concept for a skin stiffener system is presented in Figure 2. The element topology for this case (see Figure 3)
 64 is composed of three different entities; these are the nodes at the top surface of the skin, at the bottom
 65 surface of the stiffener and the floating connectors that ensure the connection for a given stiffener position.
 66 The FC element also incorporates in its formulation an optimization algorithm to adaptively re-position the
 67 stiffener along the skin based on a chosen objective function (presented in Section 4).

68 Although we will explore in this paper the use of the floating connector element for design optimisation
 69 problems, the concept itself can also be used to investigate the effect of manufacturing defects. For instance,
 70 in the skin-stifener problem, the element can readily introduce debonding between stiffener and skin by
 71 removing the appropriate floating connectors in order to simulate a kissing bond, or to investigate the most
 72 critical areas for debonding location.

73 *2.2. Mathematical formulation*

74 To represent the connection between the respective n_{skn} skin and n_{stf} stiffener nodes, we can start by
 75 defining suitable MPC equations. Consider the stiffener DoFs \mathbf{q}^{stf} and skin DoFs \mathbf{q}^{skn} involved in these
 76 equations and arranged in a vector $\mathbf{q}^{\text{T}} = \left[(\mathbf{q}^{\text{skn}})^{\text{T}} \quad (\mathbf{q}^{\text{stf}})^{\text{T}} \right]$. The overall MPC equation system

$$\mathbf{L}\mathbf{q} = \mathbf{0}, \tag{1}$$

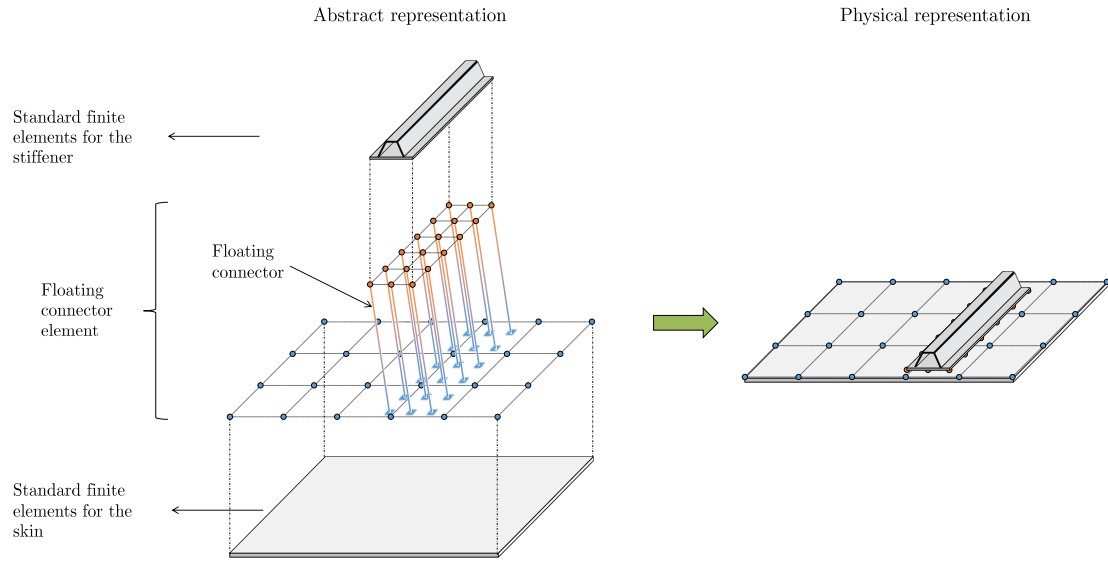


Figure 2: The floating connector element creates an evolving physical connection between two separate components, even if they are spatially ‘distant’ in the FE model

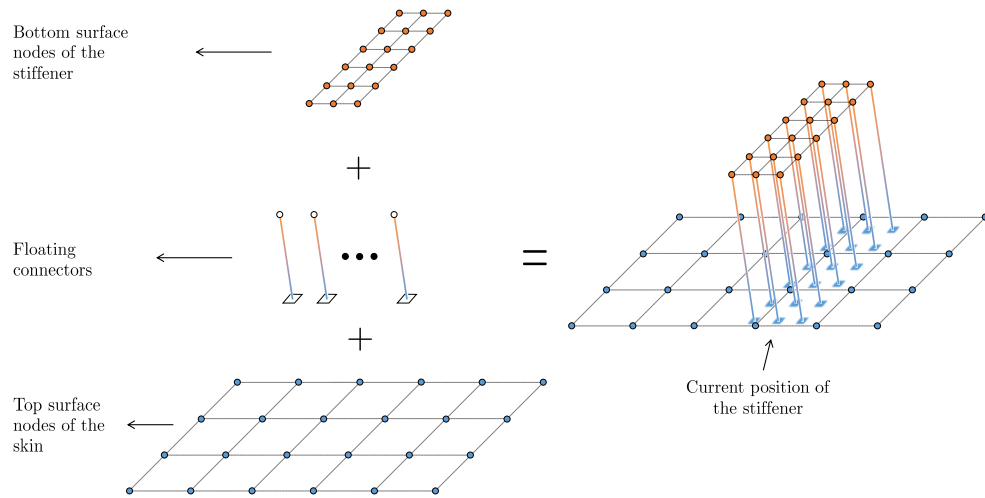


Figure 3: Floating connector element topology

77 contains a coefficient matrix \mathbf{L} with sub-matrices \mathbf{L}^{stf} and \mathbf{L}^{skn} relative to the stiffener and skin DoFs
 78 respectively:

$$\mathbf{L} = \begin{bmatrix} \mathbf{L}^{\text{skn}} & \mathbf{L}^{\text{stf}} \end{bmatrix}, \quad (2)$$

79 To define the coefficient matrix \mathbf{L} , and as shown in Figure 4, we consider a skin element with domain Ω^e , n^e
80 nodes and shape function N_i^e ($i = 1, 2, \dots, n^e$), as well as a node k from the stiffener with position \mathbf{x}_k that
81 should be connected to the skin and overlaps this element domain Ω^e . The MPC equation (which can be
82 used to define the DoFs of node k as a function of the DoFs of the skin element) can then be written as

$$\sum_{i=1}^{n^e} \mathbf{N}_i^e \mathbf{q}_i - \mathbf{q}_k = \mathbf{0}, \quad (3)$$

83 where the DoFs, expressed in a coordinate system x , y and z , as

$$\mathbf{q}_i^T = \begin{bmatrix} q_i^x & q_i^y & q_i^z \end{bmatrix} \text{ and} \quad (4)$$

$$\mathbf{q}_k^T = \begin{bmatrix} q_k^x & q_k^y & q_k^z \end{bmatrix}, \quad (5)$$

84 and $\mathbf{N}_i^e = N_i^e \mathbf{I}_3$ where \mathbf{I}_3 is the identity matrix with size 3. Noting Equation 3 can be expanded over all
85 nodes n_{skn} of the skin:

$$\sum_{i=1}^{n_{\text{skn}}} \mathbf{N}_i^e \mathbf{q}_i - \mathbf{q}_k = \mathbf{0}. \quad (6)$$

86 Noting Equations 1, 2 and 6, it is clear that the matrices \mathbf{L}^{skn} and \mathbf{L}^{stf} are defined as

$$\mathbf{L}^{\text{skn}} = \begin{bmatrix} \mathbf{a}_{11} & \cdots & \mathbf{a}_{1i} & \cdots & \mathbf{a}_{1n_{\text{skn}}} \\ \vdots & \ddots & \vdots & \ddots & \vdots \\ \mathbf{a}_{k1} & \cdots & \mathbf{a}_{ki} & \cdots & \mathbf{a}_{kn_{\text{skn}}} \\ \vdots & \ddots & \vdots & \ddots & \vdots \\ \mathbf{a}_{n_{\text{stf}}1} & \cdots & \mathbf{a}_{n_{\text{stf}}i} & \cdots & \mathbf{a}_{n_{\text{stf}}n_{\text{skn}}} \end{bmatrix} \text{ and } \mathbf{L}^{\text{stf}} = -\mathbf{I}_{n_{\text{stf}}} \quad (7)$$

87 with

$$\mathbf{a}_{ki} = \begin{cases} \mathbf{N}_i^e(\mathbf{x}_k) & \Leftarrow \mathbf{x}_k \subset \Omega^e \\ \mathbf{0} & \Leftarrow \mathbf{x}_k \not\subset \Omega^e \end{cases}, \text{ and} \quad (8)$$

88 where $\mathbf{I}_{n_{\text{stf}}}$ is the identity matrix of size n_{stf} . Having defined the MPC equations, we then integrate them
89 into the FC element using a penalty stiffness formulation. Considering the constraints \mathbf{g}_c given by

$$\mathbf{g}_c = \mathbf{L}\mathbf{q} = \mathbf{0}, \quad (9)$$

90 the Courant quadratic penalty energy can be expressed as

$$U_p = k_p |\mathbf{g}_c|^2 = k_p \mathbf{q}^T \mathbf{L}^T \mathbf{L} \mathbf{q}, \quad (10)$$

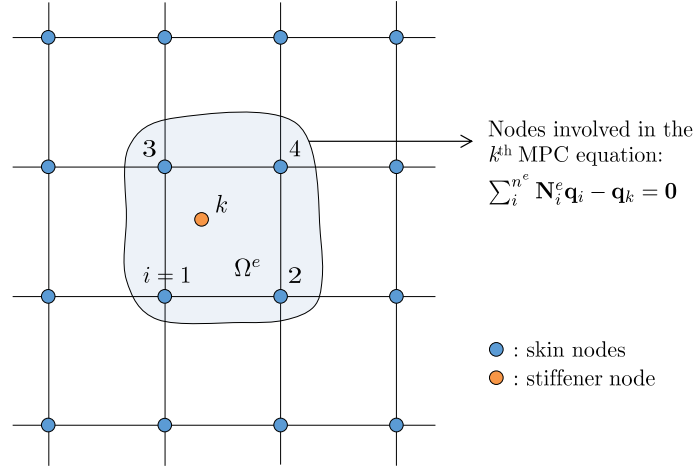


Figure 4: MPC implementation

91 where k_p is the penalty stiffness. Then, minimization with respect to the DoFs yields the element stiffness
 92 matrix \mathbf{K}_p as

$$\mathbf{K}_p = k_p \mathbf{L}^T \mathbf{L}, \quad (11)$$

93 with the internal force vector \mathbf{f}_p given by

$$\mathbf{f}_p = \mathbf{K}_p \mathbf{q}. \quad (12)$$

94 It is worth noting that the concept of floating connector element is not restricted to the penalty stiffness
 95 method. Other methods (e.g. such as Augmented Lagrangian or cohesive zone modelling) can also be used
 96 and the element stiffness can be derived accordingly.

97 This formulation can be readily implemented in a user-defined element subroutine in a typical finite
 98 element code and integrated into a numerical model composed of standard finite elements accounting for
 99 the skin and stiffener parts. This point is worth emphasizing: the floating connector element is defined
 100 independently of the two components it connects; hence these two components can be modelled directly
 101 using any element types available to the modeller in a particular finite element software, with the floating
 102 connector elements being simply added afterwards.

103 The implementation of the element in a commercial FE software starts with the creation of an FE model
 104 for each different level (the skin and stiffener in our case). The individual skin and stiffener models are
 105 introduced into the same simulation platform where they can be positioned in any location. An input file
 106 that contains all the information for nodes, elements, and connectivities is generated via the commercial
 107 FE software. Then, using a pre-processing code, all the nodes of the skin and stiffener that can potentially
 108 interact are extracted from the input file. In our case, these nodes include the nodes on the bottom surface

109 of the stiffener and the top surface of the skin. Using these nodes (in particular their nodal number),
110 a user-defined element corresponding to the floating connector element is constructed (element nodes are
111 specified) and added into the input file. The modified input file is used to start the simulation where the
112 user-element code performs the FE calculations for the floating connector element, whereas the commercial
113 software performs calculations for the standard elements. The use of a floating connector element is therefore
114 relatively straight-forward. More importantly, it can also potentially be incorporated in standard FE pre-
115 processors, making its use as trivial as using as contact algorithm.

116 **3. Verification of the floating connection**

117 *3.1. Introduction*

118 In order to confirm that the proposed floating connector element correctly represents the connection
119 between two components, we implemented it in Abaqus [24] and defined a verification test case where we
120 compared the elastic response of models using the floating connector to that of models using standard built-in
121 tie constraints. To this end, a skin-stiffener system as shown in Figure 5a was simulated with the geometrical
122 dimensions given in Figure 5b and Table 1. In this verification case, the skin was exposed to 10 MPa pressure
123 loading at the top surface and the design variable is the position x of the stiffener (Figure 5b). The edges
124 of the skin and stiffener are clamped as illustrated in Figure 5a. The skin and stiffener parts are composed
125 of uni-directional plies with quasi-isotropic stacking sequence and 0.125 mm. The skin and the stringer part
126 of the stiffener (see Figure 5b) has a stacking sequence of $[0/-45/45/90]_{2s}$ whereas the stiffener foot has
127 $[0/-45/45/90]_s$. The material properties of the plies are provided in Tables 2 and 3. The Courant penalty
128 stiffness was chosen as 10^8 N/mm^3 .

129 We created two different models using either solid or shell meshes (the solid mesh is shown in Figure 6),
130 and in both cases verified that the results were mesh converged. We ran one simulation using the floating
131 connector element so that the stiffener sweeps different positions x (see Figure 5b), and recorded the corre-
132 sponding maximum deflection of the skin. We then ran several simulations (one for each stiffener position)
133 using instead the standard built-in tie constraints available in Abaqus [24], and repeated the whole process
134 using solid (Section 3.2) and shell (Section 3.3) elements. The results for these case are provided Sections 3.2
135 and 3.3.

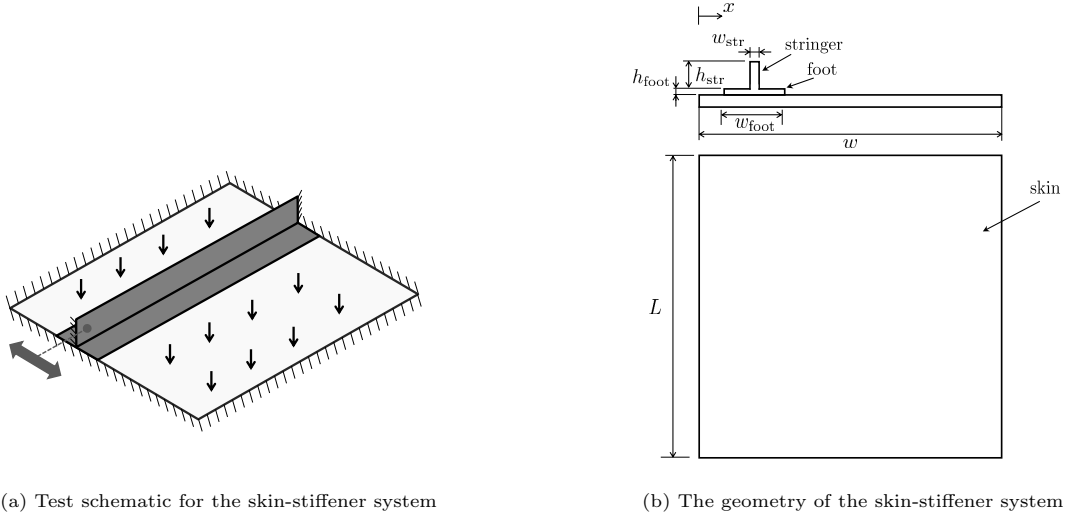


Figure 5: Skin-stiffener system schematic and geometry

Table 1: Geometry of the skin-stiffener system

| Description | Symbol | Value (mm) |
|--------------------|-----------------------|------------|
| Panel length | l | 100 |
| Panel width | w | 100 |
| Stringer width | w_{stringer} | 20 |
| Stringer height | h | 9 |
| Panel thickness | t | 2 |
| Stringer thickness | t_{stringer} | 2 |
| Foot thickness | t_{stringer} | 1 |

Table 2: Elasticity related material properties for IM7-8552 [25]

| E_{11} (GPa) | $E_{22} = E_{33}$ (GPa) | $\nu_{12} = \nu_{13}$ | ν_{23} | $G_{12} = G_{13}$ (GPa) | G_{23} (GPa) |
|----------------|-------------------------|-----------------------|------------|-------------------------|----------------|
| 161 | 11.38 | 0.32 | 0.44 | 5.17 | 3.98 |

Table 3: Fracture and strength related material properties for IM7-8552 [25]

| G_{Ic} (kJ/m ²) | G_{IIc} (kJ/m ²) | η |
|-------------------------------|--------------------------------|--------|
| 0.21 | 0.77 | 2.1 |

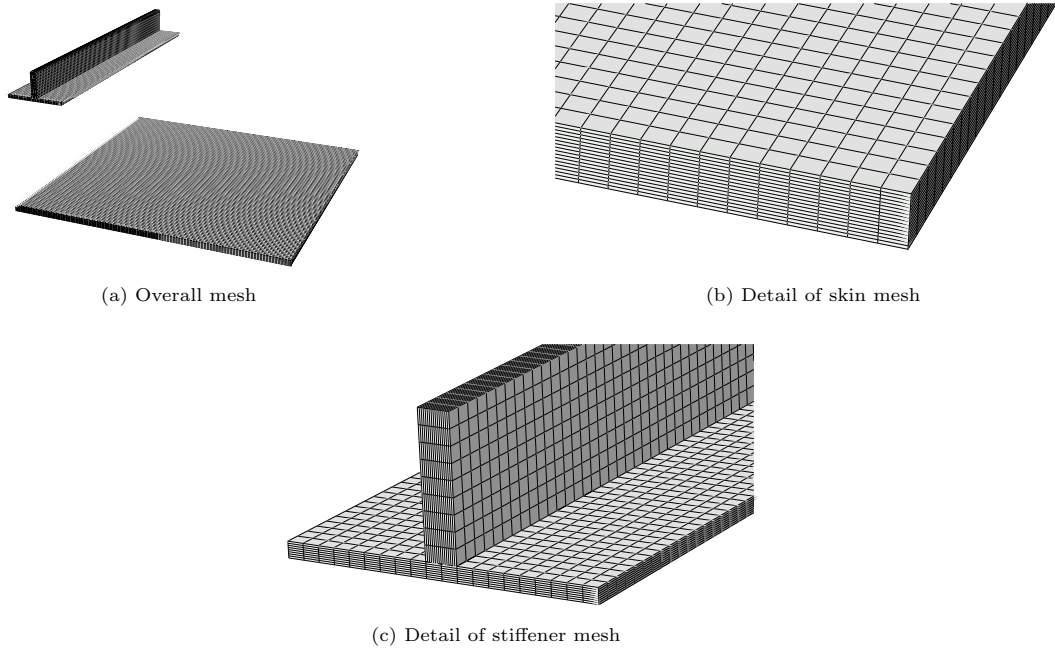


Figure 6: The mesh composed of solid elements for the verification simulation

136 *3.2. Solid to solid connection*

137 For the model with solid elements, we used solid hexahedral elements with linear shape functions (C3D8).
 138 All of the elements in the model have dimensions of 1 x 1 x 0.125 mm such that each ply is represented
 139 with one element in the thickness. We verified that this mesh size leads to mesh-converged results. The
 140 maximum skin deflection for each stiffener position is shown in Figure 7.

141 For the simulation with the floating connector element, Figure 8 illustrates the evolution of the mesh as
 142 the status of the floating connector element represents a connection between the stiffener and the skin at
 143 different positions x . Together, Figures 7 and 8 demonstrate that the floating connector element correctly
 144 represents the connection between solid components.

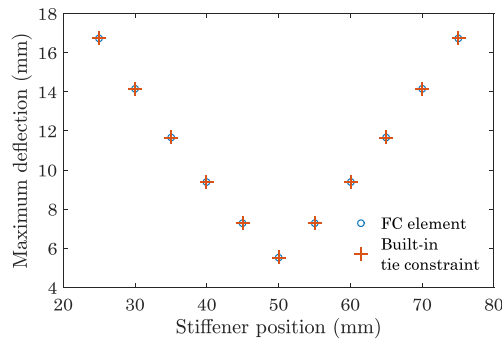


Figure 7: Maximum skin deflection vs. stiffener position predictions using solid elements in the component parts

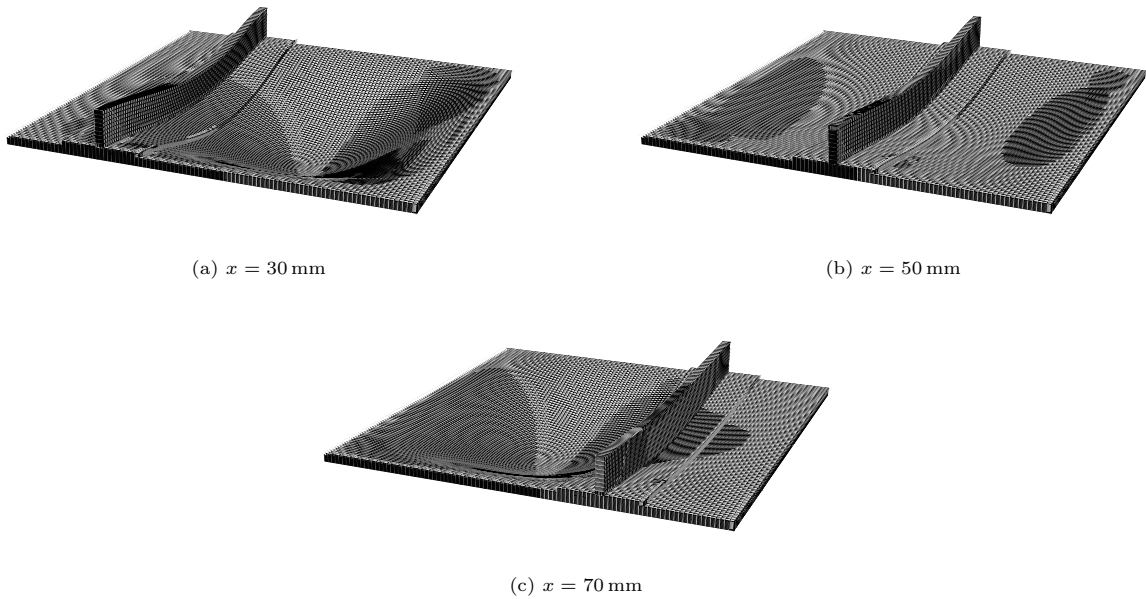


Figure 8: The status of the floating connector element allows us to represent a stiffener at any desired position for the model composed of solid elements. All sub-figures were obtained from one single simulation. (Note that, for visualisation purposes, the stiffener in these images is a dummy stiffener with negligible stiffness and with MPC equations used to deform it as the real stiffener and to shift it to the correct value of x .)

145 3.3. Shell to shell connection

146 For the model with shell elements, we used 4-noded shell elements (S4) with the dimensions of 1 x 1 mm.
 147 Again we verified that this mesh size produces mesh-converged results. The maximum skin deflection for
 148 each stiffener position is shown in Figure 9.

149 For the simulation with the floating connector element, Figure 10 shows the evolution of the mesh as
 150 the status of the floating connector element represents a connection between the stiffener and the skin at
 151 different positions x . From Figures 9 and 10, we observe that the floating connector element correctly applies
 152 the connection between components composed of shell elements as well.

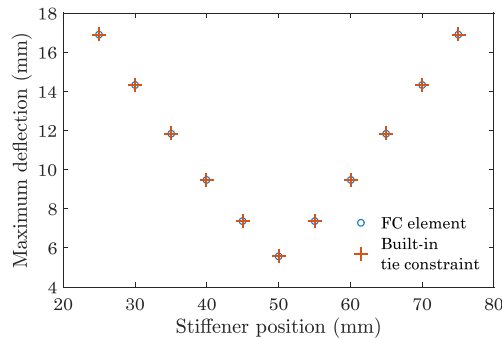


Figure 9: Maximum skin deflection vs. stiffener position predictions using shell elements in the component parts

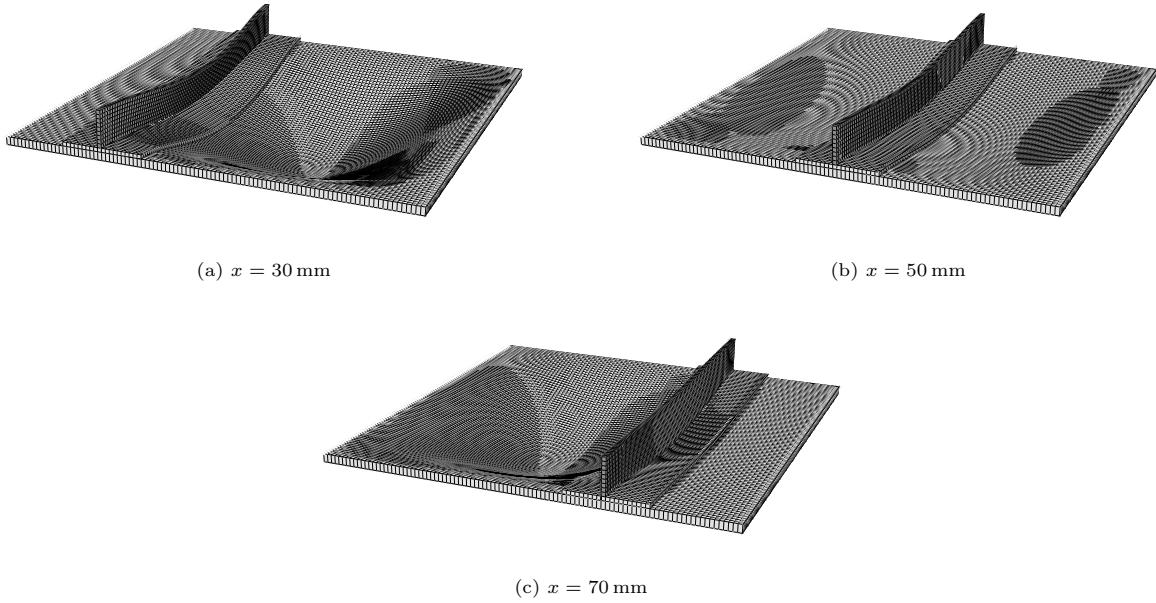


Figure 10: The status of the floating connector element allows us to represent a stiffener at any desired position for the model composed of shell elements. All sub-figures were obtained from one single simulation. (Note that, shell thickness's were rendered to better show the contact). For visualisation purposes, the stiffener in these images is a dummy stiffener with negligible stiffness and with MPC equations used to deform it as the real stiffener and to shift it to the correct value of x , and the shell thicknesses were rendered to better show the contact.)

153 4. Optimization

154 4.1. Introduction

155 In order to demonstrate the adaptive connection capability of the FC element, different optimizations
 156 algorithms can be integrated to the element formulation to attain the optimum stiffener location along the
 157 skin based on a chosen objective function (minimum skin deflection in this case). We implemented two
 158 of these algorithms, namely gradient descent and genetic algorithm, and the respective descriptions are
 159 provided in Sections 4.2 and 4.3.

160 4.2. Gradient descent

161 In gradient descent optimization, the gradient of the function intended to be optimized (cost function J)
 162 with respect to a system parameter θ is used to direct the solution to a local minimum point. The generic
 163 formulation can be written as

$$\theta_k = \theta_{k-1} - \eta \cdot \nabla_{\theta} J(\theta_{k-1}), \quad (13)$$

164 where k refers to the step number, η is the learning rate and $\nabla_{\theta} J(\theta_{k-1})$ is the gradient of J with respect to
 165 θ evaluated at step $k - 1$. For the specific verification case we choose, the equation becomes

$$x_k^{\text{stf}} = x_{k-1}^{\text{stf}} - \eta \nabla_{x^{\text{stf}}} J(x_{k-1}^{\text{stf}}), \text{ with} \quad (14)$$

$$J(x^{\text{stf}}) = \delta^{\text{skn}}(x^{\text{stf}}), \quad (15)$$

166 where x^{stf} is the stiffener position and $\delta^{\text{skn}}(x^{\text{stf}})$ is the absolute value of the maximum deflection of the skin
 167 surface for a stiffener at position x^{stf} . In this algorithm, the gradient part determines the direction whereas
 168 the learning rate determines the step size for the parameter update. Considering the chosen skin-stiffener
 169 system, in order to calculate the gradient, a finite difference scheme can be used:

$$\nabla_{x^{\text{stf}}} J(x_{k-1}^{\text{stf}}) \approx \frac{J(x_{k-1}^{\text{stf}}) - J(x_{k-2}^{\text{stf}})}{x_{k-1}^{\text{stf}} - x_{k-2}^{\text{stf}}}. \quad (16)$$

170 At each iteration, the integrated gradient descent algorithm of the element uses the current deformed state
 171 and determines the stiffener position for the next iteration of the numerical analysis.

172 Using this algorithm, the maximum deflection vs. stiffener position during the various iterations of the
 173 analysis are provided in Figure 11a. In the current implementation, the learning rate is set as 10mm and
 174 divided by 4 each time the algorithm overshoots the extrema point. This effectively means modifying the
 175 learning rate when the gradient changes its sign resulting in excellent convergence (see Figure 11b). An
 176 animation of the combined mechanical-optimisation study with this gradient descent method is given as
 177 [extra material](#) with this paper.

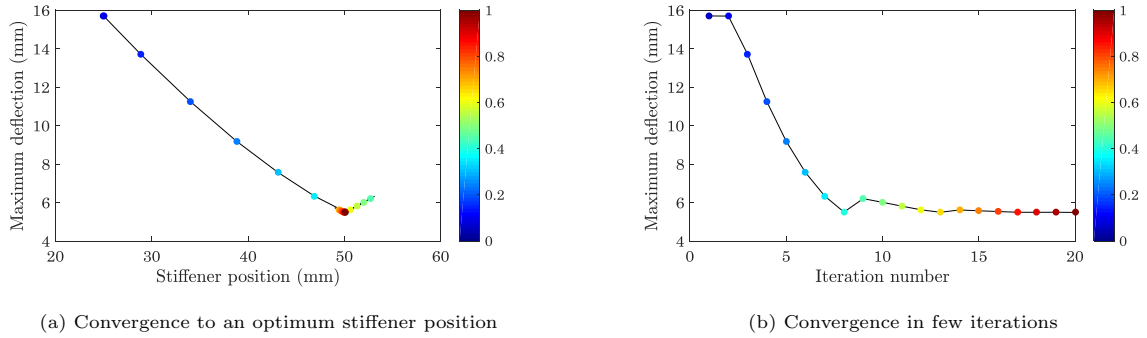


Figure 11: The gradient descent method implemented within a FC element leads to a combined mechanical-optimisation problem which converges in few iterations (the colour of the circles represents the normalized iteration number)

178 4.3. Genetic algorithm

179 4.3.1. Introduction

180 The genetic algorithm implemented within the FC element (see Figure 12) is briefly explained in this
 181 section. For more details on genetic algorithms, the reader is referred to the literature [26, 27]. The

182 genetic algorithm (see Figure 12) involves several steps: population initialization; fitness calculation; parent
183 selection; crossover; mutation; survivor selection; and termination. Before the explaining these, some key
184 terminology is described first in Section 4.3.2.

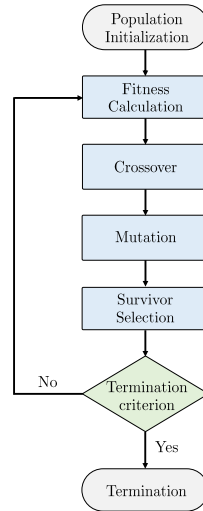


Figure 12: Genetic algorithm structure

185 4.3.2. Key terminology

186 A genetic algorithm enables finding the optimum solution, starting from a given set of individual so-
187 lutions, using operations such as crossover and mutation inspired by biological evolution. The set of such
188 possible individual solutions of the problem is referred as the population (see Figure 13).

189 The actual representation of the solutions of a system that corresponds to a real-life instance (e.g. stiffener
190 positions given as real numbers) are referred to as ‘phenotype’ representation. In order to apply the genetic
191 algorithm operations, the solutions however need to be represented in an encoded form which is referred to
192 as ‘genotype’ representation. The encoded representation of each solution is called a chromosome, and this
193 is composed of genes. The genes represent one element of the encoded sequence of a chromosome and the
194 value it takes is called an allele (see Figure 13).

195 In order to assess the optimality of each solution, we need a fitness function which assigns a certain
196 numerical value to the solution based on a measure of its performance. Thus, the fitness function operates
197 on the phenotype representation to assess the optimality of the solution.

198 As mentioned, the main genetic operations are ‘crossover’ and ‘mutation’. ‘Crossover’ generates a new
199 generation of solutions by blending the genetic information of selected chromosomes in the previous gener-
200 ation whereas ‘mutation’ modifies the allele of the genes based on a low mutation probability.

201 During the genetic algorithm operations, the fitness function operates on the phenotype representation

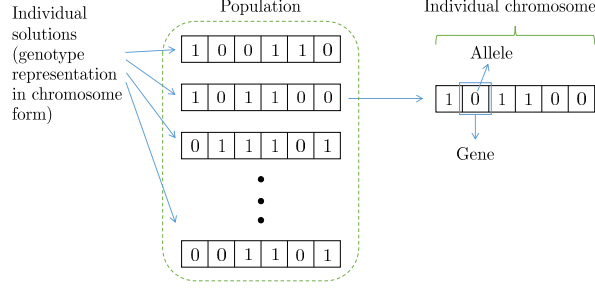


Figure 13: Genetic algorithm terminology

202 to assess the optimality of the solutions. Then, the phenotype representation is converted to a genotype
 203 representation to run the crossover and mutation operations. The new chromosomes that are generated in
 204 each generation then need to be decoded back to phenotype representation to calculate their fitness value.
 205 Thus, in order to convert between the various representations, suitable encoding and decoding operations
 206 are essential.

207 In the current implementation of the algorithm, a binary representation is used for the encoding. Con-
 208 sidering a given interval for the stiffener position $x^{\text{stf}} \subset [x_{\text{in}}, x_{\text{fn}}]$, each of the real-valued solutions x^{stf} can
 209 be represented as a binary number with $n_{\text{bt}} \in \mathbb{N}$ digits. Thus, the overall solution space can contain up to
 210 $2^{n_{\text{bt}}}$ distinct solutions. Consider a binary representation of a solution as

$$(x^{\text{stf}})_2^{\text{bn}} = (b_{n_{\text{bt}}-1} b_{n_{\text{bt}}-2} \cdots b_i \cdots b_2 b_1 b_0), \quad (17)$$

211 where b_i refers to the individual digit numbers in binary form with $b_i \in \{0, 1\}$. The genetic algorithm
 212 operates on the sequences (chromosomes) $(x^{\text{stf}})_2^{\text{bn}}$ which correspond to each individual solution x^{stf} .

213 In order to convert real valued representation (phenotype) into chromosome form (genotype), first, each
 214 of the n_{ppl} admissible stiffener position x^{stf} can be represented as an integer in the interval $[0, 2^{n_{\text{bt}}}]$ as

$$(x^{\text{stf}})^{\text{bn}} = (2^{n_{\text{bt}}} - 1) \frac{x^{\text{stf}} - x_{\text{in}}}{x_{\text{fn}} - x_{\text{in}}}, \quad (18)$$

215 which can be written in the binary form $(x^{\text{stf}})_2^{\text{bn}}$ shown in Equation 3, hence defining the bits b_i .

216 Equally, using the binary representation $(x^{\text{stf}})_2^{\text{bn}}$, the real-valued solutions x^{stf} can be recovered using:

$$(x^{\text{stf}})^{\text{bn}} = \sum_{i=1}^{n_{\text{bt}}} b_i 2^{i-1}, \quad (19)$$

$$x^{\text{stf}} = x_{\text{in}} + (x^{\text{stf}})^{\text{bn}} \cdot \frac{x_{\text{fn}} - x_{\text{in}}}{2^{n_{\text{bt}}} - 1}. \quad (20)$$

217 The resolution Δx that can be achieved with n_{bt} digits for the binary number is therefore:

$$\Delta x = \frac{x_{in} - x_{fn}}{2^{n_{bt}} - 1}. \quad (21)$$

218 4.3.3. Population initialization

219 Population initialization refers to the initial seeding that corresponds to various solutions x_j^{stf} in the
220 search space

$$X_0^{stf} = \left\{ x_1^{stf}, x_2^{stf}, \dots, x_j, \dots, x_{n_{ppl}}^{stf} \right\}, \quad (22)$$

221 where $n_{ppl} \leq 2^{n_{bt}}$ refers to the number of solutions in the population. The seeding can be realized in various
222 ways, e.g. uniformly or randomly. In the uniform case, the initial population is distributed over the solution
223 space uniformly while, in the random case, a random bit $b_{ij} \in 0, 1$ is assigned to the individual bit i of each
224 individual solution j of the population with $1 \leq i \leq n_{bt}$ and $1 \leq j \leq n_{ppl}$. In this work, we used $n_{ppl} = 10$
225 and $n_{bt} = 8$ for both the verification in Section 4 and the application in Section 5.

226 4.3.4. Fitness calculation

227 To assess the fitness of each solution, the respective output is calculated and a fitness value is assigned
228 to determine the probability that the solution can contribute its genetic information to the next generation
229 of solutions. The fitness value needs to be higher for fitter individuals in the population.

230 Additionally, it is convenient for the forthcoming calculation of probabilities that the fitness values are
231 all non-negative. With this in mind, let δ_j^{skn} be the absolute value of the maximum deflection of the skin
232 for solution j (corresponding to a stiffener position x_j^{stf}). Thus, a suitable fitness function can be:

$$F_j = -\delta_j^{skn} + c, \quad (23)$$

233 with

$$c = \max_{j \in \{1, n_{ppl}\}} \{ \delta_j^{skn} \}. \quad (24)$$

234 Alternatively, we can use Equation 23 to define the rank of each solution x_j^{stf} and then define the fitness of
235 x_j^{stf} as

$$F_j = n_{ppl} + 1 - \text{rank}(x_j^{stf}). \quad (25)$$

236 In this work, we used this latter approach throughout.

237 4.3.5. Parent selection

238 After the fitness calculation, the probability of a solution contributing to the next generation is calculated.
239 With the fitness function being higher for fitter solutions, and always non-negative, the probability of a

240 solution j being selected to contribute to the next generation is

$$P_j = F_j/F_T, \quad (26)$$

241 with

$$F_T = \sum_{j=1}^{n_{\text{ppl}}} F_j. \quad (27)$$

242 This probability is then used repeatedly to select sets of two parents. The process for selecting each
243 parent consists of the following:

- 244 (i) generating a random number $r \in [0, F_T]$;
- 245 (ii) starting from the first individual ($j = 1$) summing the fitness values until the summation exceeds the
246 number r ; and
- 247 (iii) the last individual solution included in the summation is chosen as a parent.

248 Graphically, this process can be visualised as spinning a Roulette wheel divided in n_{ppl} segments cor-
249 responding to each individual solutions, and with the length of each segment being proportional to the
250 respective fitness (Figure 14). Finally, the parents are arranged in sets of 2, with each set being used to
251 generate two children.

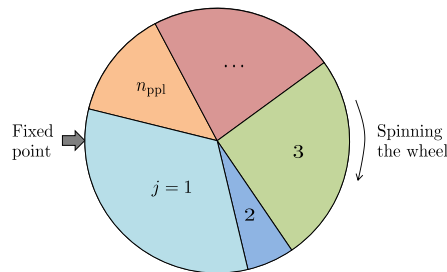


Figure 14: Roulette wheel selection

252 4.3.6. Crossover

253 ‘Crossover’ refers to the operation whereby parent chromosomes contribute certain portion of their genetic
254 information to the children population. In the current implementation (see Figure 15a), a one point crossover
255 was used. In this approach, two parent chromosomes are selected and divided at a random section. Then,
256 the divided parts up to and after the random section from the two parents are switched to preliminarily
257 define two children chromosomes.

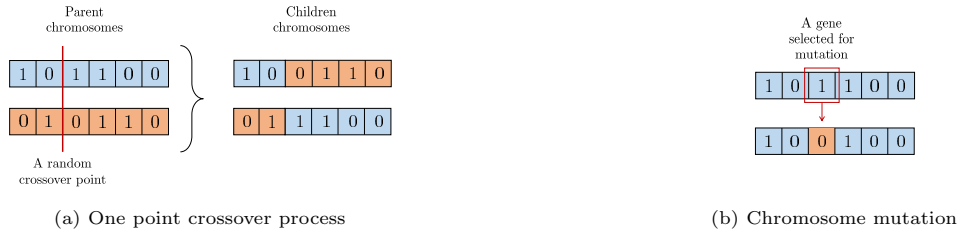


Figure 15: Genetic algorithm operations

258 4.3.7. Mutation

259 Once the children chromosomes have been preliminary defined, a mutation operation is applied to some
 260 genes, according to a pre-defined small probability P_{mt} , so as to diversify the population and explore the
 261 solution space. In the current implementation, we use bit flip mutation for the mutation operation. In this
 262 approach, if a certain gene is selected for mutation based on a low probability, its bit number (allele) is
 263 flipped (see Figure 15b). In this work, we used $P_{mt} = 10\%$.

264 Additionally, for each generation, if we observe multiple numbers of exactly the same chromosome, we
 265 apply a mutation with 100% probability on the first half of the digits of the chromosomes (i.e. for b_0 to b_3
 266 in our case in which we have $n_{bt} = 8$) to introduce diversity to the population and reduce crowding.

267 4.3.8. Survivor selection

268 To define the next generation of solutions, we retain the top $n_{rm} < n_{ppl}$ solutions of the previous
 269 generation, and replace the remaining $n_{ch} = n_{ppl} - n_{rm}$ solutions with the children solutions previously
 270 generated. In this work, we used $n_{ch} = 5$.

271 4.3.9. Termination

272 The algorithm can be terminated either using a suitable clustering criterion, or when a certain number
 273 of generations n_{gen} has been created. Regarding the former, a suitable convergence criterion is to require
 274 that a certain fraction f of the solutions are closer to each other than a certain tolerance ϵ . In our case, we
 275 used $n_{gen} = 100$. Additionally, for the verification in Section 4 and the application in Section 5, we used
 276 $f = 80\%$ and $\epsilon = 2$ mm.

277 4.3.10. Verification

278 We applied genetic algorithm optimisation to the stiffener problem defined in Section 3.1. The change
 279 of the stiffener position for each generation is provided in Figure 16. As it can be expected from a genetic
 280 algorithm, the solutions corresponding to the different members of the population start to cluster around the
 281 optimum point. An animation of the concurrent mechanical-optimization study with this genetic algorithm
 282 is given as [extra material](#) with this paper.

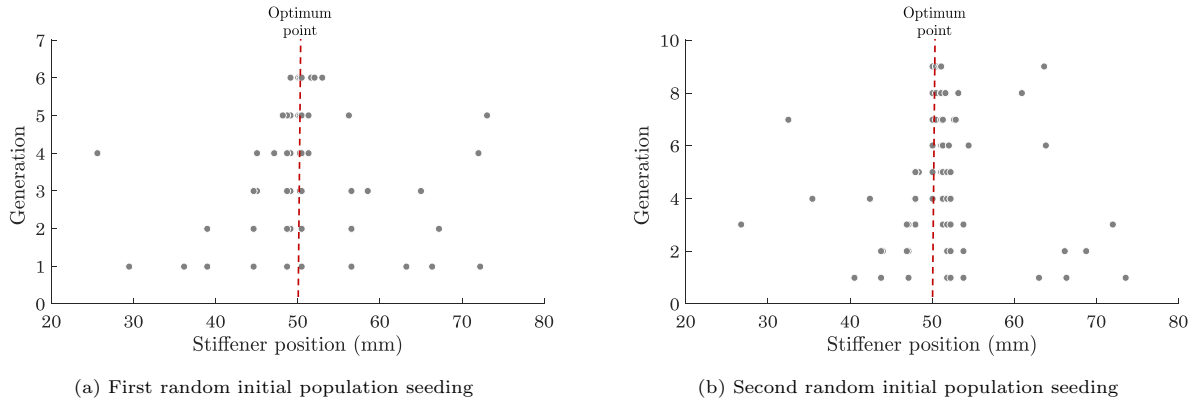


Figure 16: Combined mechanical-optimisation simulation of the position of a stiffener, using FC elements and a genetic algorithm, showing clustering at the optimal position for two different random seedings of the initial population

283 5. Application

284 5.1. Introduction and problem definition

285 This paper introduced a novel FC element which enables coupled mechanical-optimisation finite element
 286 simulations. We now apply this novel methodology to a meaningful engineering problem (Figure 17): the
 287 positioning a runout stiffener on a plate, so as to minimise the deflection of the plate while not exceeding the
 288 critical energy release for debonding of the runout. We consider that the runout contains a manufacturing
 289 defect, i.e. an initial debonding representative of the minimum debond size that cannot be identified via
 290 inspection.

291 The runout problem shown in Figure 17 is similar to the problem introduced in Section 3.1 (i.e. same
 292 material and same geometry where applicable). The only differences are that there is a runout, with the
 293 stiffener being $\ell_{\text{stf}} = 90$ mm long, with a runout region $\ell_{\text{ro}} = 10$ mm long and with a debond length
 294 $\ell_{\text{db}} = 10$ mm. The applied pressure is $p = 210$ kPa. To be conservative, we require that the maximum total
 295 energy release rate at any point along the debond must be lower than the mode I critical energy release rate.

296 5.2. Numerical model and formulation

297 To model the skin-stiffener system, hexahedral solid elements were used with linear shape functions,
 298 except at the runout section where solid tetrahedral elements with linear shape function are assigned.

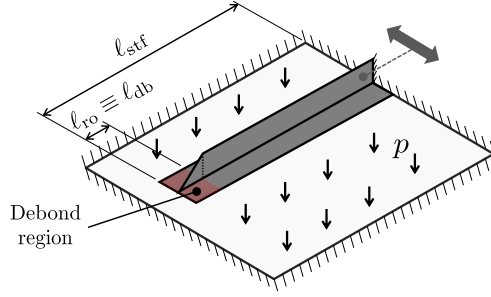


Figure 17: Application test schematic and geometry

299 Using the FC element formulation, the manufacturing defect (initial debonding of the runnout) can be
 300 introduced readily. This is achieved by de-activating the floating connectors (see Section 2.2) which operate
 301 on the stiffener nodes along the debonded region.

302 Debonds can be modelled efficiently using various techniques, including cohesive elements [28–39] and
 303 VCCT [9, 10, 25, 40, 41]. In this work, we will use the latter. In order to implement the constraint of no
 304 debond growth, the energy release rates at the debond front need to be calculated. Using the virtual crack
 305 closure technique [40] (VCCT), the energy release rates in mode I, II and III (G_I , G_{II} , and G_{III} , respectively)
 306 at a certain node along the debond front can be given as

$$G_I = -\frac{1}{2\ell_a\ell_b} F_n \llbracket q_n^W \rrbracket, \quad (28)$$

$$G_{II} = -\frac{1}{2\ell_a\ell_b} F_s \llbracket q_s^W \rrbracket, \text{ and} \quad (29)$$

$$G_{III} = -\frac{1}{2\ell_a\ell_b} F_t \llbracket q_t^W \rrbracket, \quad (30)$$

307 where ℓ_a and ℓ_b refer to the element in-plane dimensions, F_\bullet are the components of the nodal forces at the
 308 node on the debond front and $\llbracket q_\bullet^W \rrbracket$ represent the components of the separation in the wake of the debond
 309 front. The subscripts n , s and t refer (using standard notation) to the local coordinate of the debond for
 310 which the VCCT forces and separations are calculated [40].

311 Within the FC element subroutine, the separations at the wake of the debond and the forces at the
 312 debond front can be readily calculated. From Equation 3, the separation vector $\llbracket \mathbf{q}_k \rrbracket$ for a node k can be
 313 written as

$$\llbracket \mathbf{q}_k \rrbracket = \mathbf{q}_k - \sum_i^{n^e} \mathbf{N}_i^e \mathbf{q}_i. \quad (31)$$

314 Equation 31 can be used directly to calculate the separations in the wake of the debond front $\llbracket q_\bullet^W \rrbracket$ in
 315 Equations 28, 29 and 30. The nodal forces for the corresponding node at the debond front can be calculated
 316 from the relevant components of the separation vector at the debond front ($\llbracket q_\bullet^{DF} \rrbracket$), using again Equation 31

317 and the Courant quadratic penalty stiffness k_p of the element (see Equation 10) as:

$$F_n = k_p \llbracket q_n^{\text{DF}} \rrbracket, \quad (32)$$

$$F_s = k_p \llbracket q_s^{\text{DF}} \rrbracket, \text{ and} \quad (33)$$

$$F_t = k_p \llbracket q_t^{\text{DF}} \rrbracket. \quad (34)$$

318 According to the problem definition in Section 5.1, the (conservative) constraint for the validation case is
 319 then $G_T < G_{\text{Ic}}$ where G_T is the total energy release rate along the debond front given as $G_T = G_{\text{I}} + G_{\text{II}} + G_{\text{III}}$.
 320 This constraint needs to be evaluated at each node along the debond front.

321 We show the solution to the constrained optimization problem using the genetic algorithm route only,
 322 as the solution using gradient descent is equivalent. In the genetic algorithm, the solutions which do not
 323 verify the constraint are given zero fitness.

324 5.3. Results

325 The evolution of the stiffener position over various generations is provided in Figure 18. The initial
 326 geometry and final deformation of the skin-stiffener system is also given in Figure 19. An animation of the
 327 combined mechanical-optimization study for this runout problem is given as [extra material](#) with this paper.
 328 The results show that the optimum position for the stiffener is at $x^{\text{stf}} \approx 63$ mm. Note that the problem
 329 is not exactly symmetric due to the laminated nature of the components (e.g. the 45° plies are not at the
 330 same height in the laminate thickness as the -45° plies); as a result, while there is a local optimum on the
 331 left of Figure 18, the absolute optimum is on the right. As the system is not isotropic, equilibrium occurs
 332 at a non-symmetric stiffener position where the clustering happens.

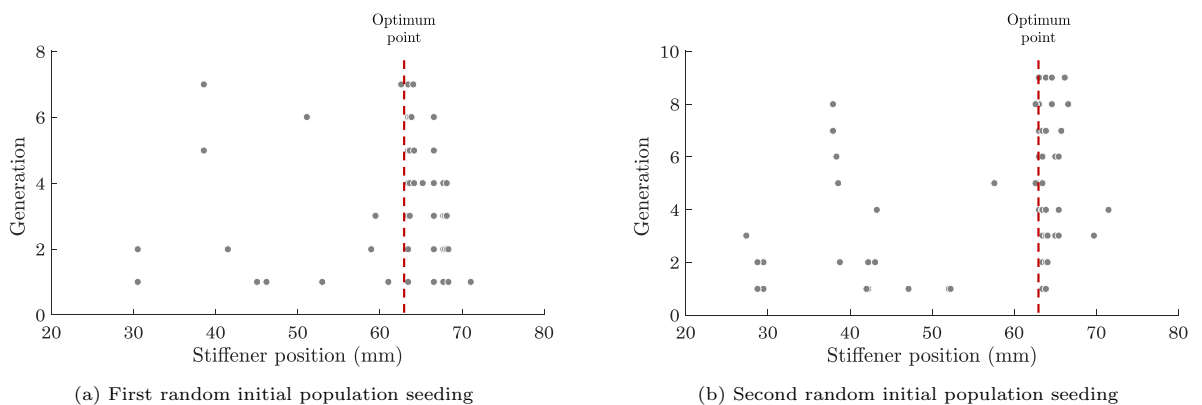
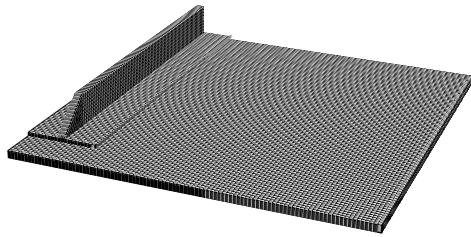
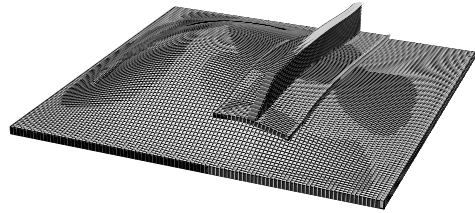


Figure 18: Combined mechanical-optimisation simulation of the position of a stiffener runout, using FC elements and a genetic algorithm, showing clustering at the optimal position for two different random seedings of the initial population. The simulation solves the mechanical problem and optimises for minimum deflection, with a constraint on maximum energy release rate.



(a) Initial status of the skin-stiffener system



(b) Final status for the skin-stiffener system where the stiffener is positioned at the optimal position $x^{\text{stf}} \approx 63$ mm

Figure 19: The stiffener position evolves naturally to the optimal position during the constrained combined mechanical-optimisation analysis

333 6. Discussion

334 The verification results (Figures 7 and 9) show the newly proposed FC element accurately captures the
 335 connection between two generic structural components. This provides a new route for adaptively connecting
 336 different components within a finite element simulation.

337 When used to sweep the design domain, as shown in Section 3, the FC simulation route can simulate
 338 numerous configurations without needing to create separate finite element analyses, without modifying the
 339 overall geometry of the model, without re-meshing the components, and in fact without even needing to
 340 recompute the individual stiffness matrices of the individual components. In comparison, sweeping the
 341 design domain using manual or scripted model generation would have none of these advantages.

342 The potential reduction in the overall simulation time depends on the number of configurations n_{cf} that
 343 need to be simulated. The methodology requires only one model generation step at the beginning of the
 344 simulation.

345 Moreover, it is important to emphasise that the model provides a versatile simulation platform where
 346 different levels can be configured and integrated on-the-fly inside one finite element analysis. This enables
 347 the user to investigate the levels in a more effective manner without switching between different FE models
 348 and software.

349 The optimization results (Sections 4 and 5 and additional material) show that the FC element is able
 350 to integrate different optimization algorithms into its formulation. When a gradient descent algorithm is
 351 activated within the FC element, the simulation successfully reaches the desired optimum (Figure 11 and
 352 [extra material](#)). When a genetic algorithm is activated within the FC element, the simulation converges to a
 353 cluster around the desired optimal (Figure 16 and [extra material](#)). When the optimization problem includes
 354 constraints, the simulation converges to a cluster on one side of the desired optimal (as expected because of
 355 the constraint).

356 The application in Section 5 demonstrates three further points. Firstly, it demonstrates that the FC
357 element approach can also deal with constrained optimisation problems in relevant engineering applications.
358 Secondly, it demonstrates that the FC element can readily be used to perform fracture mechanics calcula-
359 tions, in this case using VCCT (although modelling decohesion using a cohesive element approach would
360 be possible as well). Thirdly, it demonstrates that, in addition to being used for configurational design
361 problems, FC elements can also readily be used to analyse the effect of defects in engineering structures. In
362 this case, we analysed the effect of a debond of a fixed size; in general, other manufacturing defects could
363 be considered and the design variables could instead search for maximum allowable defects.

364 7. Conclusions

365 We formulated an original Floating Connector (FC) element that enables adaptive positioning of lower-
366 level models (such as components) within higher level-models (such as large structures) in a single FE model.
367 The conclusions from this paper are:

- 368 • this new FC element formulation can lead to a combined mechanical/optimisation problem for the
369 design of multi-level structures (such as the positioning of stiffeners within a wingbox);
- 370 • the combined mechanical/optimisation approach does not require re-generating the geometry, remesh-
371 ing or modifying the stiffness matrix of the elements in the FE model enabling significant time reduction
372 particularly for complex models;
- 373 • FC elements can be implemented as user-elements in standard FE software packages with a user-
374 element interface;
- 375 • FC elements can integrate a variety of optimisation algorithms, including gradient descent and genetic
376 algorithms;
- 377 • FC elements allow naturally the incorporation of manufacturing defects (or other pre-existing damage)
378 in the connection between the different hierarchical levels (e.g. debondings) and optimisation taking
379 their existence into account; and
- 380 • FC element can also potentially be used to determine maximum allowable manufacturing defects given
381 a specific performance requirement.

382 The conclusions above imply that this new FC element provides a versatile simulation platform with on-
383 the-fly multi-level configuration capability. It enables significant user time reduction, particularly for large
384 problems and where a large number of configurations need to be considered. The methodology therefore
385 opens new avenues for more effective structural design with significantly less user input.

386 Acknowledgement

387 The first author greatly acknowledges the scholarship from The Scientific and Technological Research
388 Council of Turkey (TUBITAK) and British Council Turkey in the framework of the programmes BIDEB-
389 2213 and Newton-Katip Celebi Fund. The third author is grateful for the funding form EPSRC under grant
390 EP/M002500/1.

391 Data availability

392 The raw/processed data required to reproduce these findings cannot be shared at this time as the data
393 also forms part of an ongoing study.

- 394 [1] J. Reinoso, A. Blázquez, A. Estefani, F. París, J. Cañas, E. Arévalo, F. Cruz, Experimental and three-dimensional global-
395 local finite element analysis of a composite component including degradation process at the interfaces, *Composites Part*
396 *B* 43 (2012) 1929–1942.
- 397 [2] J. Reinoso, A. Blázquez, A. Estefani, F. París, J. Canas, A composite runout specimen subjected to tension–compression
398 loading conditions: Experimental and global–local finite element analysis, *Compos. Struct.* 101 (2013) 274–289.
- 399 [3] Y. Sato, T. Okabe, R. Higuchi, K. Yoshioka, Multiscale approach to predict crack initiation in unidirectional off-axis
400 laminates, *Adv. Compos. Mater* 23 (2014) 461–475.
- 401 [4] S. Hühne, J. Reinoso, E. Jansen, R. Rolfes, A two-way loose coupling procedure for investigating the buckling and damage
402 behaviour of stiffened composite panels, *Compos. Struct.* 136 (2016) 513–525.
- 403 [5] M. Akterskaia, E. Jansen, S. Hühne, R. Rolfes, Efficient progressive failure analysis of multi-stringer stiffened composite
404 panels through a two-way loose coupling global-local approach, *Compos. Struct.* 183 (2018) 137–145.
- 405 [6] M. Akterskaia, E. Jansen, S. R. Hallett, P. Weaver, R. Rolfes, Analysis of skin-stringer debonding in composite panels
406 through a two-way global-local method, *Compos. Struct.* 202 (2018) 1280–1294.
- 407 [7] S. Guinard, R. Bouclier, M. Toniolli, J.-C. Passieux, Multiscale analysis of complex aeronautical structures using robust
408 non-intrusive coupling, *Advanced Modeling and Simulation in Engineering Sciences* 5 (2018) 1.
- 409 [8] R. McCune, C. Armstrong, D. Robinson, Mixed-dimensional coupling in finite element models, *Int. J. Numer. Methods*
410 *Eng.* 49 (2000) 725–750.
- 411 [9] R. Krueger, J. Ratcliffe, P. Minguet, Panel stiffener debonding analysis using a shell/3d modeling technique, *Compos.*
412 *Sci. Technol.* 69 (2009) 2352–2362.
- 413 [10] R. Krueger, T. O’Brien, A shell/3d modeling technique for the analysis of delaminated composite laminates, *Composites*
414 *Part A* 32 (2001) 25–44.
- 415 [11] H. B. Dhia, G. Rateau, The arlequin method as a flexible engineering design tool, *Int. J. Numer. Methods Eng.* 62 (2005)
416 1442–1462.
- 417 [12] L. Gigliotti, S. Pinho, Multiple length/time-scale simulation of localized damage in composite structures using a mesh
418 superposition technique, *Compos. Struct.* 121 (2015) 395–405.
- 419 [13] P. R. Budarapu, J. Reinoso, M. Paggi, Concurrently coupled solid shell-based adaptive multiscale method for fracture,
420 *Comput. Methods Appl. Mech. Eng.* 319 (2017) 338–365.
- 421 [14] E. Kocaman, B. Chen, S. Pinho, A polymorphic element formulation towards multiscale modelling of composite structures,
422 *Comput. Methods Appl. Mech. Eng.* 346 (2019) 359–387.
- 423 [15] R. Degenhardt, A. Kling, K. Rohwer, A. Orifici, R. Thomson, Design and analysis of stiffened composite panels including
424 post-buckling and collapse, *Computers & Structures* 86 (2008) 919–929.

- 425 [16] R. Zimmermann, H. Klein, A. Kling, Buckling and postbuckling of stringer stiffened fibre composite curved panels—tests
426 and computations, *Compos. Struct.* 73 (2006) 150–161.
- 427 [17] R. Yondo, E. Andrés, E. Valero, A review on design of experiments and surrogate models in aircraft real-time and
428 many-query aerodynamic analyses, *Prog. Aerosp. Sci.* 96 (2018) 23–61.
- 429 [18] R. Rikards, H. Abramovich, K. Kalnins, J. Auzins, Surrogate modeling in design optimization of stiffened composite
430 shells, *Compos. Struct.* 73 (2006) 244–251.
- 431 [19] P. Badalló, D. Trias, E. Lindgaard, Damage tolerance optimization of composite stringer run-out under tensile load,
432 *Compos. Struct.* 133 (2015) 98–104.
- 433 [20] N. V. Queipo, R. T. Haftka, W. Shyy, T. Goel, R. Vaidyanathan, P. K. Tucker, Surrogate-based analysis and optimization,
434 *Prog. Aerosp. Sci.* 41 (2005) 1–28.
- 435 [21] L. Lamberti, S. Venkataraman, R. T. Haftka, T. F. Johnson, Preliminary design optimization of stiffened panels using
436 approximate analysis models, *Int. J. Numer. Methods Eng.* 57 (2003) 1351–1380.
- 437 [22] V. M. F. Correia, M. A. A. Gomes, A. Suleman, C. M. M. Soares, C. A. M. Soares, Modelling and design of adaptive
438 composite structures, *Comput. Methods Appl. Mech. Eng.* 185 (2000) 325–346.
- 439 [23] D. Systèmes, 5.7 documentation (isight), Providence, RI: Dassault Systèmes (2012).
- 440 [24] D. Systèmes, Abaqus 6.14 documentation, Providence, RI: Dassault Systèmes (2014).
- 441 [25] R. Krueger, Development and application of benchmark examples for mixed-mode i/ii quasi-static delamination propa-
442 gation predictions, NASA/CR-2012-217562, NASA, 2012 (2012).
- 443 [26] M. Mitchell, An introduction to genetic algorithms, MIT press, 1998.
- 444 [27] K. Deb, An introduction to genetic algorithms, *Sadhana* 24 (1999) 293–315.
- 445 [28] L. F. Kawashita, S. R. Hallett, A crack tip tracking algorithm for cohesive interface element analysis of fatigue delamination
446 propagation in composite materials, *Int. J. Solids Struct.* 49 (2012) 2898–2913.
- 447 [29] L. F. Kawashita, A. Bedos, S. R. Hallett, Modelling mesh independent transverse cracks in laminated composites with a
448 simplified cohesive segment method, *Computers, Materials, & Continua* 32 (2012) 133–158.
- 449 [30] F. Van der Meer, L. Sluys, A phantom node formulation with mixed mode cohesive law for splitting in laminates, *Int. J.*
450 *Fract.* 158 (2009) 107.
- 451 [31] F. Van Der Meer, L. Sluys, The thick level set method: sliding deformations and damage initiation, *Comput. Methods*
452 *Appl. Mech. Eng.* 285 (2015) 64–82.
- 453 [32] A. Ahmed, F. Van der Meer, L. Sluys, A geometrically nonlinear discontinuous solid-like shell element (dsls) for thin shell
454 structures, *Comput. Methods Appl. Mech. Eng.* 201 (2012) 191–207.
- 455 [33] S. Pinho, L. Iannucci, P. Robinson, Formulation and implementation of decohesion elements in an explicit finite element
456 code, *Composites Part A* 37 (2006) 778–789.
- 457 [34] P. P. Camanho, C. Davila, S. Pinho, Fracture analysis of composite co-cured structural joints using decohesion elements,
458 *Fatigue & fracture of engineering materials & structures* 27 (2004) 745–757.
- 459 [35] P. Areias, J. Song, T. Belytschko, Analysis of fracture in thin shells by overlapping paired elements, *Comput. Methods*
460 *Appl. Mech. Eng.* 195 (2006) 5343–5360.
- 461 [36] B. Chen, T. Tay, S. Pinho, V. Tan, Modelling the tensile failure of composites with the floating node method, *Comput.*
462 *Methods Appl. Mech. Eng.* 308 (2016) 414–442.
- 463 [37] E. Barbieri, M. Meo, A meshfree penalty-based approach to delamination in composites, *Composites Science and*
464 *Technology* 69 (2009) 2169–2177.
- 465 [38] E. V. Iarve, M. R. Gurvich, D. H. Mollenhauer, C. A. Rose, C. G. Dávila, Mesh-independent matrix cracking and
466 delamination modeling in laminated composites, *International journal for numerical methods in engineering* 88 (2011)
467 749–773.

- 468 [39] K. Hoos, E. V. Iarve, M. Braginsky, E. Zhou, D. H. Mollenhauer, Static strength prediction in laminated composites by
469 using discrete damage modeling, *Journal of Composite Materials* 51 (2017) 1473–1492.
- 470 [40] R. Krueger, Virtual crack closure technique: history, approach, and applications, *Appl. Mech. Rev.* 57 (2004) 109–143.
- 471 [41] A. Riccio, M. Gliotti, A novel numerical delamination growth initiation approach for the preliminary design of damage
472 tolerant composite structures, *Journal of composite materials* 41 (2007) 1939–1960.